S1. Supplementary

In the following sections, we describe the instrumentation of GC×GC–ToF-MS sensor, the compound peak detectors introduced in [11], including a detailed overview of our custom CNN architecture. We also present comprehensive results for the baseline method developed by analytical chemists [6], and for the deterministic descriptors.

S1.1. Sensor Instrumentation

Analyses were conducted on an Agilent 7890B gas chromatograph (Agilent, Santa Clara, CA, USA) coupled to time-of-flight mass spectrometers Pegasus® 4D-C and Pegasus® BT-4D (LECO Corp., St. Joseph, MI, USA). Automated sample introduction was performed with a MultiPurpose Sampler MPS Robotic (Gerstel, Mülheim, Germany). Raw data were exported from the ChromaTOF® software (versions 4.72.0.0, 5.51.06.0, and 5.55.41_BT; LECO Corp., St. Joseph, MI, USA).

The GC×GC–ToF-MS configuration followed a previously reported layout [26] employing a reverse column arrangement: a medium-polar primary column Rtx-200MS (Restek, Bellefonte, PA, USA, 30 m × 0.25 mm × 0.25 μm) and a non-polar secondary column TG-5HT (Thermo Fisher Scientific, Waltham, MA, USA, 1 m × 0.25 mm × 0.25 μm). Of the total secondary-column length, 10 cm were located in the modulator, 69 cm in the secondary oven, and 21 cm in the GC-MS transfer line. A 2 m pre-column of the same stationary phase as the primary column was installed. When using the Pegasus BT-4D detector, the secondary column totaled 1.1 m to accommodate 31 cm within the GC-MS transfer line.

Prior to injection, samples were homogenized by shaking for 10 min followed by 10 min in an ultrasonic bath. Injections of 1 μL were made with a 1 μL air plug in the syringe, at 280°C in splitless mode (2 min splitless time). Carrier gas was operated at a constant-flow rate of 1.5 mL/min. The oven program was: 40°C (2 min), ramp at 5°C/min to 320°C (10 min), for a total runtime of 68 min (4080 s). The secondary oven was maintained at +5°C relative to the primary oven and the modulator at +20°C relative to the primary. Cryogenic modulation of the secondary column used dried air at -80°C. The run comprised three modulation segments: 500-1704 s (period 6 s; hot pulse 1.8 s; cold pulse 1.2 s), 1704-2592 s (period 8 s; hot 2.4 s; cold 1.6 s), and 2592-4080 s (period 10 s; hot 3.3 s; cold 1.7 s).

The transfer line was held at 280°C and the ion source at 250°C. Electron ionization (EI) at 70 eV was used. Total ion current (TIC) data were collected over m/z 29–800 at 200 spectra s^{-1}. The acquisition delay was 500 s, and the detector voltage was set 200 V above the tuned value to enhance sensitivity.

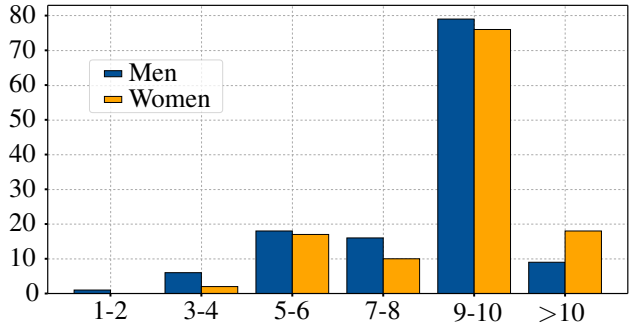

Figure S1. Histogram of measurement counts per identity in the HSD dataset, grouped by biological sex (see Sec. 4). X-axis: measurements per identity, y-axis: number of subjects.

Dataset	Total num.	n	Number of samples per identity min	max	avg	median
4D-C	504	40	10	37	12.6	10
HSD	2528	252	1	76	10.0	10

Table S1. Dataset statistics. From left to right: dataset name, total number of samples, number of identities n in the dataset, and: (i) minimum, (ii) maximum, (iii) average, and (iv) median number of measurements per identity.

S1.2. Compound Peak Detectors

We locate the characteristic peak of each compound using an annotated 4D-C dataset of 40 individuals (504 total samples) from [11, 25]. Although we train our compound-peak detectors on a small annotated set, we subsequently rectify the entire Human Scent Dataset (Sec. 4) using these learned detectors, eliminating the need for extensive annotation by chemical experts. To align the spectral resolutions, we quantized the high-spectral-resolution measurements to match the dimensions of the low-spectral-resolution data. We then stored the detected peak positions and applied the registration procedure to each channel representation using these stored positions.

S1.2.1. Chemical Compounds Being Detected

In the registration step, we followed [11] exactly. We used the set of 22 chemical compounds from the paper and also experimented with the addition of two more compounds, Heptacosane and Nonacosane. See the list of compounds in Table S2. Note that a standardized mass spectrum of all listed compounds is available in public databases.

S1.2.2. Bounding Box Constraint

Many compounds share similar mass spectra (see Fig. 1), so *positional cues* are crucial as discussed in [11]. We restrict the search for compound c to a bounding box around its

#	Compound
1	Tetradecane, 1-chloro-
2	2,5-pyrrolidinedione, 3-decyl-
3	2,5-pyrrolidinedione, 3-dodecyl-
4	2,5-pyrrolidinedione, 3-tetradecyl-
5	2,5-pyrrolidinedione, 3-hexadecyl-
6	Squalene
7	Cholesterol
8	Cholesta-3,5-dien-7-one
9	Cholest-4-en-3-one
10	Cholesta-4,6-dien-3-one
11	Hexadecanoic acid, dodecyl ester
12	9-Hexadecenoic acid, tetradecyl ester
13	Hexadecanoic acid, tetradecyl ester
14	9-Hexadecenoic acid, hexadecyl ester
15	Hexadecanoic acid, hexadecyl ester
16	9-Hexadecenoic acid, octadecyl ester
17	Hexadecanoic acid, octadecyl ester
18	1-Dodecanol
19	Dodecane, 1-chloro-
20	Dodecanamide, N-allyl-
21	Fumaric acid, 2-dimethylaminoethyl heptyl ester
22	Cholesta-3,5-diene (isomer 2)
23	Heptacosane
24	Nonacosane

Table S2. List of compounds used for registration in our experiments, following [11]. The first 22 compounds correspond to the set actually used for registration in [11]. Heptacosane and Nonacosane were only mentioned in the original paper but not used there; in our experiments, we evaluated both the 22-compound and 24-compound variants.

average position $\overline{\mathbf{u}}_c$:

$$\mathrm{BBox}\big(\overline{\mathbf{u}}_c, w, h\big) \;= \tag{S1}$$

$$= \Big\{ \mathbf{u} \in \Omega \;\Big|\; \big|\overline{u}_{1,c} - u_1\big| < \tfrac{w}{2}, \quad \big|\overline{u}_{2,c} - u_2\big| < \tfrac{h}{2} \Big\}, \tag{S2}$$

where $\Omega := \{1, \dots, H\} \times \{1, \dots, W\}$ is the pixel grid, and w, h are the bounding-box dimensions.

S1.2.3. Weighted Cosine Peak Detector

Cosine similarity alone can yield spurious matches. To reduce those, we apply a spatial penalty that was presented in [11]:

$$\hat{\mathbf{u}}_c^{c_{\cos}(\overline{\mathbf{u}}_c, \overline{\mathbf{s}}_c)} \;=\; \arg \max_{\mathbf{u} \,\in\, \mathrm{BBox}\left(\overline{\mathbf{u}}_c\right)} \Big[\cos\big(\overline{s}_c,\, s_{\mathbf{u}}\big) \;-\; p\big(\overline{\mathbf{u}}_c,\, \mathbf{u}\big) \Big],$$

where

$$p\big(\overline{\mathbf{u}}_c,\, \mathbf{u}\big) \;=\; \big(\,|\overline{u}_{1,c} - u_1| \;+\; 6\,|\overline{u}_{2,c} - u_2| \big)^4.$$

The exponent $(\cdot)^4$ strongly penalizes large deviations, and the factor of 6 accounts for typically wider shifts along the first chromatographic dimension. This detector thus prefers spectra near $\overline{\mathbf{u}}_c$ that match $\overline{s}_c$.

Cosine similarity measures the angular alignment between two spectra, making the approach invariant to absolute intensity scaling.

S1.2.4. Fully Convolutional Network (FCN) Peak Detector

A fully convolutional network (FCN) that was shown in [11] predicts *class likelihood* at each pixel. Let Ω_c be the set of pixels classified by the FCN as belonging to compound c. We combine the FCN prediction with cosine similarity:

$$\hat{\mathbf{u}}_c^{\mathrm{FCN}(\mathbf{u},\mathbf{s})^+_{\cos}} \;=\; \arg \max_{\mathbf{u} \,\in\, \Omega_c} \Big[\mathrm{FCN}\big(\mathbf{u}, s\big) \;+\; \cos\big(\overline{s}_c,\, s_{\mathbf{u}}\big) \Big].$$

In both detectors, the final peak location is the pixel $\mathbf{u}$ that maximizes the respective score.

S1.3. Canonical Frame Registration

As noted in [11], "variations in instrument conditions (e.g., temperature changes, aging, injection timing) shift compound retention times and lead to misalignment of GC×GC–ToF-MS measurements." Canonical-frame registration was therefore considered a key step in their processing pipeline. We reimplemented the procedure introduced in [11] and conducted experiments with and without registration to assess its impact in our setting.

Let $\mathcal{R}^{\mathrm{ref}} = \{c_1, c_2, \dots\}$ denote the set of reference compounds. For each $c \in \mathcal{R}^{\mathrm{ref}}$, let $\mathbf{u}_c \in \mathbb{R}^2$ be the reference location and s_c^{ref} the corresponding mass spectrum.

In each human scent sample (GC×GC–ToF-MS measurement) $\mathcal{S}$, we first detect the occurrences (see Sec. S1.2 for detectors description) of a fixed set of reference compounds (see Sec. S1.2.1 for the list). This set corresponds to the compounds that were reported as consistent across samples in [11]. For each compound $c \in \mathcal{R}^{\mathrm{ref}}$ we obtain its detected position $\mathbf{u}_c^{(\mathcal{S})} \in \mathbb{R}^2$ and corresponding mass spectrum $s_c^{(\mathcal{S})}$.

Given the detected positions $\mathcal{U}^{(\mathcal{S})} = \{\mathbf{u}_c^{(\mathcal{S})} \mid c \in \mathcal{R}\}$ in sample $\mathcal{S}$, we construct a Delaunay triangulation between $\mathcal{U}^{(\mathcal{S})}$ and reference locations $\mathcal{U}$ to establish correspondence for the registration step.

For each triangle in the Delaunay triangulation, we compute a local affine mapping that transforms the detected vertices $\mathbf{u}_{c_1}^{(\mathcal{S})}, \mathbf{u}_{c_2}^{(\mathcal{S})}, \mathbf{u}_{c_3}^{(\mathcal{S})}$ of sample $\mathcal{S}$ to the corresponding reference vertices $\mathbf{u}_{c_1}, \mathbf{u}_{c_2}, \mathbf{u}_{c_3}$. A point $\mathbf{u}^{(\mathcal{S})}$ in the measured sample is first expressed in barycentric coordinates $(\lambda_1, \lambda_2, \lambda_3)$ with respect to $(\mathbf{u}_{c_1}^{(\mathcal{S})}, \mathbf{u}_{c_2}^{(\mathcal{S})}, \mathbf{u}_{c_3}^{(\mathcal{S})})$,

$$\mathbf{u}^{\mathcal{S}} = \lambda_1 \mathbf{u}_{c_1}^{(\mathcal{S})} + \lambda_2 \mathbf{u}_{c_2}^{(\mathcal{S})} + \lambda_3 \mathbf{u}_{c_3}^{(\mathcal{S})}, \quad \lambda_1 + \lambda_2 + \lambda_3 = 1, \;\; \lambda_i \geq 0.$$

The canonical position $\mathbf{u}$ is then obtained by mapping the same barycentric coordinates to the reference triangle,

$$\mathbf{u} = \lambda_1 \mathbf{u}_{c_1} + \lambda_2 \mathbf{u}_{c_2} + \lambda_3 \mathbf{u}_{c_3}.$$

Finally, the entire human scent sample is interpolated on the transformed mesh using piecewise linear interpolation, yielding the canonical frame representation.

This process allows comparison of scent samples taken under different conditions as was introduced in [11].

S1.4. Triangular Kernel Function For Channel Representation

In addition to the Gaussian kernel function introduced in 3.2, we experimented with triangular kernel

$$\kappa_\Delta(m_n; \mu_k, w_k) = \max(1 - \frac{|m_n - \mu_k|}{w_k}, 0),$$

a piecewise linear function whose half-width $w_k > 0$ is learned. In this case, the kernel centers μ_k are set using the same heuristic as in Sec. 5.2.

We apply a 10-fold cross-validation on the dataset of 2528 samples by 497×2000 retention times by "number of spectral samples". For the Triangular kernel, we again minimize the weighted reconstruction error E (5.1.1) using stochastic gradient descent and compare two weight schemes: uniform weighting and inversed-intensity weighting (5.1.1).

κ	w	$C = 3$	$C = 5$	$C = 10$	$C = 20$
G	U	$6.3 \cdot 10^{-8}$	$1.4 \cdot 10^{-7}$	$4.5 \cdot 10^{-7}$	$3.9 \cdot 10^{-8}$
G	I	$5.1 \cdot 10^{-6}$	$1.7 \cdot 10^{-5}$	$5.1 \cdot 10^{-7}$	$8.0 \cdot 10^{-7}$
Δ	U	$2.7 \cdot 10^{-5}$	$1.7 \cdot 10^{-4}$	$2.5 \cdot 10^{-5}$	$2.1 \cdot 10^{-5}$
Δ	I	$1.5 \cdot 10^{-4}$	$1.5 \cdot 10^{-4}$	$1.6 \cdot 10^{-4}$	$1.0 \cdot 10^{-6}$

Table S3. Mean squared reconstruction error of channel representation with C kernels over 10-fold cross-validation of Human Scent Dataset (Sec. 4) with two kernel types κ (Gaussian kernel G and Triangular kernel Δ) and two weight types (uniform U and inversed intensity I). Reporting only μ.

The results are presented in Tab. S3 The reconstruction errors of triangular kernels is $\approx$ two orders of magnitude higher than the error of Gaussian kernels. We attribute this to the higher expressiveness and smoother approximation capability of the Gaussian kernel. Therefore, all results in the main paper are reported using Gaussian kernels.

S1.5. Architecture of Custom CNN

As a custom-designed feature extractor, we introduce a compact convolutional network, to realize the embedding function f. The model comprises three modules: (i) a convolutional backbone, (ii) a down-sampling stack, and (iii) a residual MLP head.

	Metric	Threshold τ_{feat}: not set	$\tau_{\text{feat}} = 0.1$	$\tau_{\text{feat}} = 0.5$
AUC	Euclidean	62.1 ± 6.5	49.6 ± 3.3	49.2 ± 2.6
	Pearson	57.7 ± 7.4	56.2 ± 6.7	55.2 ± 4.2
	Spearman	$\mathbf{79.3 \pm 6.2}$	56.1 ± 5.2	54.8 ± 2.9
TPR@5%FPR	Euclidean	13.7 ± 9.3	5.7 ± 2.0	3.7 ± 1.6
	Pearson	10.8 ± 9.7	9.8 ± 4.9	6.6 ± 2.1
	Spearman	$\mathbf{42.0 \pm 12.6}$	5.8 ± 3.5	1.4 ± 2.0

Table S4. Cross-validation Area Under ROC Curve and TPR@5%FPR of baseline method developed by analytical chemists [6] on 4D-C dataset [11].

Backbone consists of three stages, each featuring: (i) a 2D Convolution block with a kernel 2×8, stride $(1, 2)$, and padding $(0, 1)$, (ii) a Residual 2D Convolution Block that enhances feature propagation, and (iii) dropout layers with probabilities scaled by the dropout strength (i.e., 0.1, 0.2 and 0.3).

Down-sampling Module applies four sequential 2D Convolution block layers using a 5×5 kernel, stride 2, and padding 1, each followed by dropout at $0.3\times$ dropout strength to progressively reduce spatial dimensions.

Residual MLP Head maps the high-dimensional feature vector, the flattened down-sampled features, to the desired space representation, with an additional dropout of $0.5\times$ dropout strength to mitigate overfitting.

(Residual) 2D Convolution Block sequentially applies a 2D convolution, 2D batch normalization, a ReLU activation, and dropout. In its residual variant, the block adds the input element-wise to its output. When the input and output channel dimensions differ, a depth-wise 2D convolution is optionally applied to the input to ensure proper dimensionality alignment.

S1.6. Evaluation of Baseline Method Developed by Analyst Chemists

The full results of the experiment from Sec. 5.3.1 are presented in Table S4.

S1.7. Evaluation of Deterministic Descriptors

In this section, we evaluate three deterministic feature descriptors, LBP, HOG, and SIFT, and systematically analyze how their hyperparameter configurations influence verification performance. Detailed results are reported in Table S5.

For LBP, we vary the neighbourhood radius, $r \in \{1, 2, 3\}$, and examine both the *basic* (default) and *uniform* mapping schemes. The resulting feature embedding vector is a normalized histogram over the LBP codes.

	parameters				no registration		$c_{\cos}(\bar{\mathbf{u}}_c, \bar{\mathbf{s}}_c)$				$\mathrm{FCN}(\mathbf{u}, \mathbf{s})^{+}_{\cos}$			
							$\mathcal{R}^{(22)}$		$\mathcal{R}^{(24)}$		$\mathcal{R}^{(22)}$		$\mathcal{R}^{(24)}$	
	θ_1	θ_2	θ_3	θ_4	AUC	TPR@5%	AUC	TPR@5%	AUC	TPR@5%	AUC	TPR@5%	AUC	TPR@5%
HOG	8x8	6	3x3		72.4 ± 7.3	39.6 ± 8.1	74.3 ± 7.2	39.1 ± 7.8	74.4 ± 7.3	39.3 ± 7.7	75.8 ± 4.3	33.0 ± 7.2	76.6 ± 4.5	33.1 ± 7.1
	8x8	6	2x2		73.0 ± 6.6	39.1 ± 7.8	73.4 ± 6.5	38.9 ± 7.6	73.5 ± 6.6	38.9 ± 7.7	75.3 ± 3.6	31.9 ± 6.8	76.2 ± 3.7	31.8 ± 7.1
	16x16	6	3x3		71.0 ± 8.1	40.5 ± 8.4	74.2 ± 7.8	39.8 ± 8.1	74.3 ± 7.9	39.9 ± 8.2	75.2 ± 4.5	33.0 ± 7.1	75.8 ± 4.8	32.8 ± 7.1
	8x8	9	3x3		72.2 ± 7.9	39.4 ± 8.0	73.9 ± 7.9	38.8 ± 8.0	74.0 ± 7.9	39.3 ± 8.1	76.0 ± 4.9	33.4 ± 7.2	76.7 ± 5.0	33.5 ± 7.1
	16x16	6	2x2		71.4 ± 7.6	39.1 ± 7.8	73.5 ± 7.5	39.1 ± 7.8	73.6 ± 7.5	39.2 ± 7.8	75.3 ± 4.3	32.0 ± 6.8	76.2 ± 4.5	31.7 ± 6.8
	8x8	9	2x2		72.9 ± 7.1	38.5 ± 7.5	73.3 ± 7.1	38.2 ± 7.5	73.3 ± 7.2	38.5 ± 7.8	75.7 ± 4.0	32.2 ± 6.8	76.5 ± 4.2	32.2 ± 6.9
	16x16	9	3x3		71.2 ± 8.5	40.1 ± 8.3	73.9 ± 8.2	39.5 ± 8.1	74.0 ± 8.3	39.6 ± 8.2	75.2 ± 4.9	33.1 ± 7.0	75.8 ± 5.2	33.2 ± 7.2
	8x8	12	2x2		72.6 ± 7.4	38.0 ± 7.5	73.1 ± 7.4	37.7 ± 7.7	73.2 ± 7.5	38.1 ± 7.8	75.7 ± 4.3	32.5 ± 6.8	76.6 ± 4.5	32.7 ± 6.8
	8x8	12	3x3		72.0 ± 8.2	39.1 ± 7.9	73.8 ± 8.1	38.6 ± 8.0	73.9 ± 8.2	39.0 ± 8.2	76.0 ± 5.1	33.8 ± 7.3	76.7 ± 5.3	33.8 ± 7.1
	16x16	9	2x2		71.8 ± 7.8	38.8 ± 7.7	73.5 ± 7.8	38.9 ± 7.9	73.5 ± 7.9	39.1 ± 8.0	75.6 ± 4.5	32.0 ± 6.8	76.4 ± 4.8	32.1 ± 6.7
	16x16	12	3x3		71.3 ± 8.6	39.9 ± 8.3	73.8 ± 8.3	39.3 ± 8.0	73.9 ± 8.4	39.5 ± 8.2	75.2 ± 5.1	33.5 ± 7.1	75.8 ± 5.3	33.5 ± 7.1
	16x16	12	2x2		71.8 ± 8.0	38.6 ± 7.7	73.5 ± 7.9	38.9 ± 7.9	73.5 ± 8.0	39.1 ± 8.0	75.6 ± 4.7	32.5 ± 7.0	76.4 ± 4.9	32.3 ± 6.7
LBP	1	d			78.1 ± 3.2	15.8 ± 2.2	77.1 ± 2.8	15.8 ± 2.2	77.1 ± 2.8	15.5 ± 2.1	75.6 ± 3.0	16.2 ± 2.0	75.9 ± 3.0	16.0 ± 2.4
	1	u			76.9 ± 2.9	17.6 ± 2.3	75.7 ± 3.1	18.9 ± 3.2	75.7 ± 3.2	19.0 ± 3.3	76.8 ± 4.0	22.4 ± 4.3	78.1 ± 4.3	22.9 ± 4.9
	2	u			70.0 ± 3.3	19.8 ± 2.2	72.8 ± 3.4	20.8 ± 3.1	72.9 ± 3.4	20.7 ± 3.2	73.1 ± 5.0	22.2 ± 3.7	73.7 ± 5.5	21.9 ± 4.1
	3	u			67.8 ± 3.4	20.1 ± 2.9	70.9 ± 2.9	20.9 ± 3.0	71.0 ± 3.0	21.1 ± 3.1	71.3 ± 5.2	21.3 ± 3.6	71.1 ± 5.8	20.9 ± 3.9
	3	d			71.2 ± 4.9	16.4 ± 3.1	70.0 ± 5.1	16.8 ± 3.2	70.0 ± 5.1	16.7 ± 3.2	64.3 ± 4.0	15.9 ± 2.0	64.3 ± 3.8	15.9 ± 1.9
	2	d			67.6 ± 2.8	13.2 ± 1.4	65.6 ± 2.9	12.3 ± 1.1	65.7 ± 2.9	12.4 ± 1.0	61.3 ± 3.3	11.6 ± 1.2	61.4 ± 3.4	10.9 ± 1.6
SIFT	1000	0.04	20	1.6	64.1 ± 4.6	15.3 ± 3.6	63.8 ± 4.1	15.5 ± 4.0	63.4 ± 3.9	15.1 ± 3.8	59.0 ± 6.7	13.4 ± 4.0	58.2 ± 6.4	13.1 ± 4.0
	0	0.04	20	1.6	64.1 ± 4.6	15.3 ± 3.6	63.8 ± 4.1	15.5 ± 4.0	63.4 ± 3.9	15.1 ± 3.8	59.0 ± 6.7	13.4 ± 4.0	58.2 ± 6.4	13.1 ± 4.0
	1000	0.04	20	1.2	61.2 ± 5.6	14.7 ± 3.9	61.1 ± 5.0	14.9 ± 4.2	60.8 ± 5.1	14.6 ± 4.0	56.7 ± 6.6	12.3 ± 4.1	56.6 ± 6.2	12.5 ± 3.8
	0	0.04	20	1.2	61.2 ± 5.6	14.7 ± 3.9	61.1 ± 5.0	14.9 ± 4.2	60.8 ± 5.1	14.6 ± 4.0	56.7 ± 6.6	12.3 ± 4.1	56.6 ± 6.2	12.5 ± 3.8
	1000	0.04	10	1.6	53.2 ± 5.8	12.3 ± 3.8	59.2 ± 5.3	14.4 ± 3.2	59.1 ± 5.2	14.5 ± 3.3	56.1 ± 7.5	13.9 ± 4.2	55.5 ± 7.1	13.3 ± 4.1
	0	0.04	10	1.6	53.2 ± 5.8	12.3 ± 3.8	59.2 ± 5.3	14.4 ± 3.2	59.1 ± 5.2	14.5 ± 3.3	56.1 ± 7.5	13.9 ± 4.2	55.5 ± 7.1	13.3 ± 4.1
	1000	0.01	20	1.6	60.1 ± 7.3	17.2 ± 5.3	59.1 ± 7.3	16.8 ± 5.5	58.9 ± 7.4	16.8 ± 5.2	58.8 ± 7.0	15.5 ± 4.6	59.4 ± 6.9	15.6 ± 4.7
	0	0.01	20	1.6	60.1 ± 7.3	17.1 ± 5.3	59.2 ± 7.3	16.6 ± 5.3	59.0 ± 7.4	16.6 ± 5.1	59.2 ± 7.0	15.5 ± 4.6	60.1 ± 6.9	16.1 ± 5.0
	1000	0.01	20	1.2	63.7 ± 7.2	17.9 ± 5.2	60.1 ± 7.3	16.8 ± 4.8	60.1 ± 7.3	16.7 ± 4.8	61.4 ± 6.7	15.4 ± 4.1	62.1 ± 6.4	15.8 ± 3.8
	0	0.01	20	1.2	63.8 ± 7.1	17.8 ± 5.2	60.7 ± 7.2	16.8 ± 4.7	60.6 ± 7.2	16.7 ± 4.7	62.7 ± 6.7	16.5 ± 4.9	63.8 ± 6.5	17.4 ± 4.9
	1000	0.01	10	1.2	66.6 ± 6.0	18.6 ± 5.3	58.7 ± 7.0	16.8 ± 5.2	58.5 ± 6.9	16.3 ± 5.1	58.4 ± 7.2	15.1 ± 4.8	58.5 ± 7.2	15.5 ± 4.8
	0	0.01	10	1.2	66.6 ± 6.0	18.5 ± 5.3	58.7 ± 7.0	16.8 ± 5.1	58.5 ± 6.9	16.3 ± 5.0	58.5 ± 7.2	15.0 ± 4.7	58.8 ± 7.2	16.0 ± 5.0
	1000	0.04	10	1.2	55.0 ± 5.8	13.2 ± 3.4	57.4 ± 5.5	13.6 ± 3.6	57.2 ± 5.7	13.4 ± 3.4	54.6 ± 7.2	12.5 ± 3.7	54.4 ± 6.8	12.6 ± 4.1
	0	0.04	10	1.2	55.0 ± 5.8	13.2 ± 3.4	57.4 ± 5.5	13.6 ± 3.6	57.2 ± 5.7	13.4 ± 3.4	54.6 ± 7.2	12.5 ± 3.7	54.4 ± 6.8	12.6 ± 4.1
	0	0.01	10	1.6	56.7 ± 8.1	17.1 ± 5.5	56.1 ± 7.3	16.7 ± 5.2	56.0 ± 7.4	16.5 ± 5.1	55.6 ± 7.3	15.4 ± 4.8	56.1 ± 7.4	16.2 ± 5.5
	1000	0.01	10	1.6	56.7 ± 8.1	17.1 ± 5.5	56.1 ± 7.3	16.7 ± 5.2	56.0 ± 7.4	16.5 ± 5.1	55.6 ± 7.3	15.4 ± 4.8	56.1 ± 7.4	16.2 ± 5.5
NN					85.8 ± 5.1	39.0 ± 11.8	$\mathbf{88.0 \pm 3.1}$	$\mathbf{48.3 \pm 9.2}$	$\boldsymbol{88.0 \pm 3.6}$	$\boldsymbol{50.5 \pm 10.5}$	87.9 ± 3.5	49.1 ± 8.9	87.4 ± 2.9	50.2 ± 9.1

Table S5. Validation AUC and TPR@5%FPR for non-registered and registered data and LBP, HOG, and SIFT descriptors, and our custom CNN using single-channel data and 10-fold cross-validation. Results are reported as mean ± standard deviation across folds. Best AUC in bold, best TPR@5%FPR in italic bold. Parameters: LBP: θ_1 = radius, θ_2 = method (u = uniform, d = default); HOG: θ_1 = pixels per cell, θ_2 = number of orientation bins, θ_3 = cells per block; SIFT: θ_1 = number of features, θ_2 = contrast threshold, θ_3 = edge threshold, θ_4 = sigma.

- **Basic / default mapping.** The full P-bit code obtained by thresholding the P neighbours against the centre pixel is retained unchanged, producing a histogram with 2^P bins [18]. This variant preserves maximum detail but yields a high-dimensional, potentially sparse representation.
- **Uniform mapping.** Codes that contain more than two circular bit transitions $0 \leftrightarrow 1$ are merged into a single "miscellaneous" class, whereas the 58 uniform patterns (for P=8) remain distinct. The resulting 59-bin histogram reduces dimensionality by a factor of approximately seven and is empirically more robust to noise and small rotations.

For HOG, the feature embedding is a flattened vector formed by concatenating contrast-normalized histograms of gradient orientations computed across the image. We systematically vary three hyperparameters:

- **Cell size**. Each cell is a square patch of either 8×8 or 16×16 pixels in the input image.
- **Number of orientation bins**. The histogram can contain 6, 9, or 12 equally spaced bins.

				no registration		$c_{\cos}(\overline{\mathbf{u}}_c, \overline{\mathbf{s}}_c)$				FCN$(\mathbf{u}, \mathbf{s})^{+}_{\cos}$			
						$\mathcal{R}^{(22)}$		$\mathcal{R}^{(24)}$		$\mathcal{R}^{(22)}$		$\mathcal{R}^{(24)}$	
	κ	w	C	AUROC	TPR@5%	AUROC	TPR@5%	AUROC	TPR@5%	AUROC	TPR@5%	AUROC	TPR@5%
High-resolution time-of-flight mass spectrometer Pegasus® BT 4D													
custom CNN	G	I	3	89.2±3.6	57.2±8.0	90.8±3.4	57.1±9.6	91.0±2.8	58.7±8.4	80.6±5.1	37.8±9.4	80.9±5.3	35.8±9.0
custom CNN	G	I	5	88.5±3.5	54.6±6.3	86.6±4.3	51.9±6.3	87.4±4.1	52.0±6.8	77.7±4.3	34.1±7.7	78.3±4.7	33.3±10.1
custom CNN	G	I	10	89.3±3.9	54.9±9.0	89.4±2.2	55.4±6.2	89.6±3.1	55.9±5.8	79.0±4.3	35.4±14.0	80.5±5.0	37.6±10.4
custom CNN	G	I	20	**92.3±2.7**	**65.4±8.3**	91.7±2.6	62.7±8.5	92.1±2.4	62.1±7.6	84.9±5.0	44.3±11.4	83.1±4.9	41.8±11.2
custom CNN	Δ	I	3	90.4±2.5	56.8±10.5	89.0±3.3	53.5±11.6	89.0±3.1	53.7±8.6	82.2±4.4	38.6±10.9	82.1±4.4	37.8±8.8
custom CNN	Δ	I	5	90.0±4.6	61.0±12.3	90.4±3.0	58.8±8.5	89.6±3.4	57.9±10.5	82.1±4.2	40.3±5.0	82.5±4.5	40.1±5.8
custom CNN	Δ	I	10	**92.3±2.8**	**62.5±11.4**	89.7±4.6	59.6±8.9	89.9±4.8	58.8±10.2	83.3±4.6	43.3±8.6	83.0±4.9	40.2±10.8
custom CNN	Δ	I	20	91.0±2.6	59.9±6.5	91.3±2.4	58.2±6.5	91.2±2.6	59.8±8.4	81.9±4.1	38.6±9.7	81.6±4.5	37.4±9.6
custom CNN	–	–	1	90.8±3.7	59.6±8.3	91.2±2.7	59.6±8.5	91.2±2.9	59.7±7.3	82.7±4.8	39.6±9.3	82.8±5.2	40.9±7.9
Low-resolution time-of-flight mass spectrometer Pegasus® 4D-C ($\Delta = \mu_{low} - \mu_{high}$; σ omitted)													
custom CNN	G	I	3	-10.9	-22.4	-12.4	-22.9	-11.5	-22.9	-4.8	-7.4	-3.8	-4.7
custom CNN	G	I	5	-10.5	-21.6	-9.9	-19.7	-10.9	-19.8	-3.9	-5.6	-4.4	-4.0
custom CNN	G	I	10	-10.4	-17.7	-10.9	-19.6	-11.4	-20.8	-1.8	-1.9	-2.9	-4.4
custom CNN	G	I	20	-12.5	-27.8	-12.2	-26.0	-11.1	-24.1	-6.9	-10.9	-4.7	-7.9
custom CNN	Δ	I	3	-29.0	-35.1	-27.4	-35.0	-27.0	-36.2	-20.7	-23.2	-21.2	-21.6
custom CNN	Δ	I	5	-15.3	-30.8	-17.4	-29.8	-16.5	-28.9	-10.6	-14.2	-10.9	-12.3
custom CNN	Δ	I	10	-14.7	-28.3	-13.3	-27.9	-12.5	-25.8	-9.5	-14.7	-8.0	-11.5
custom CNN	Δ	I	20	-12.7	-24.8	-12.0	-22.1	-12.1	-23.3	-5.4	-6.7	-3.4	-4.4
custom CNN	–	–	1	-11.9	-22.7	-12.7	-23.4	-12.6	-22.3	-6.1	-5.7	-5.6	-6.9

Table S6. Comparison of high- and low-resolution mass spectrometry detectors. Area Under ROC Curve and TPR@5%FPR results for five spatial-alignment strategies on channel representation (Sec. 3.2) of 2D Gas Chromatography Mass Spectrometry measurements on Human Scent Dataset (Sec. 4). Results reported as $\mu \pm \sigma$ across 10 folds for *high-resolution*; *low-resolution* rows show $\Delta = \mu_{\text{low}} - \mu_{\text{high}}$ (negative, red; σ omitted). Identity verification performed with a custom-designed Convolutional Neural Network (CNN). Registration performed with weighted cosine $c_{\cos}(\overline{\mathbf{u}}_c, \overline{\mathbf{s}}_c)$ and fully convolutional-based FCN$(\mathbf{u}, \mathbf{s})^{+}_{\cos}$ compound peak detectors introduced in [11] with 22 and 24 detected compounds. Gaussian κ_G and triangular κ_Δ channel representation kernels were used with inversed-intensity I weightings for representation learning, with the number of channel representation kernels $C \in \{1, 3, 5, 10, 20\}$. In addition, a single-channel representation obtained by summing intensities across all m/z values was used as $C = 1$.

- **Block geometry** c. For contrast normalisation, neighbouring cells are grouped into rectangular blocks of either 2×2 or 3×3 cells.

For SIFT, we vary four key hyperparameters while maintaining the default number of layers per octave (3). The final feature vector is constructed by computing the mean of all local 128-dimensional SIFT descriptors, resulting in a fixed-length global representation. Specifically, we explore the following hyperparameters:

- **Number of features** $n \in \{0, 1000\}$. This parameter specifies the maximum number of keypoints retained after detection; n=0 disables the cap, whereas n=1000 limits the descriptor set to the 1000 strongest responses.
- **Contrast threshold** $f \in \{0.001, 0.04\}$. Filters out weak features in semi-uniform regions.
- **Edge threshold** $e \in \{10, 20\}$. Filters out edge-like features.

S1.8. Comparison of High- and Low-resolution Mass Spectrometers

We evaluate our custom CNN separately on the high- and low-resolution subsets of HSD (Sec. 4) (see Tab S7 for subsets statistics). For each detector, identity- and gender-aware folds are used, containing only samples from that detector. The cohorts are *not identity-paired* (only 3 identities overlap). High-resolution results are reported as $\mu \pm \sigma$ over 10 folds; low-resolution rows report $\Delta = \mu_{\text{low}} - \mu_{\text{high}}$ (with σ omitted). See Table S6.

Discussion. On Pegasus® BT 4D (high-res), the best configuration achieves $\mathbf{92.3 \pm 2.7}$ AUROC and $\mathbf{65.4 \pm 8.3}$ TPR5%FPR with G, I, C=20; Δ, I, C=10 is comparable ($92.3 \pm 2.8/62.5 \pm 11.4$). Increasing C helps up to $10-20$; a single summed channel (C=1) is already strong ($91.2 \pm 2.9/59.7 \pm 7.3$), so multi-channel yields modest gains. Registration via $\mathcal{R}^{(22)}$ or $\mathcal{R}^{(24)}$ does not improve over no reg-

istration (differences within σ), and the FCN-cosine variant is consistently lower ($\approx 8-10$ AUROC and $\approx 20-24$ TPR points behind across C). Relative to these high-res means, Pegasus® 4D-C (low-res) shows uniformly negative deltas; for G, I, C=20 the drop is -12.5 AUROC / -27.8 TPR, with the largest declines at small C and Δ kernels (e.g., C=3: $-29.0/-35.1$).

Overall, high-resolution appears more suitable for custom CNN; however, because cohorts are not matched, a *within-subject paired acquisition* (matched-pairs) study — measuring the same identities on both instruments under identical protocol and timing — is required to attribute differences to detector resolution rather than cohort/batch effects.

Detector resolution	Total num.	n	Number of samples per identity min	max	avg	median
low	1341	116	1	76	11.6	10
high	1187	139	2	34	8.5	9

Table S7. Statistics of detector-specific subsets of Human Scent Dataset. Pegasus® 4D-C is the low-resolution detector; Pegasus® BT 4D is the high-resolution detector. Columns: dataset name, number of samples, number of identities n, and per-identity counts (min, max, mean, median). See full dataset statistics in Supplementary Table S1.

S1.9. Regularization and Data Augmentation

To improve generalization under limited data, we regularized the custom CNN with dropout. In the *Backbone*, dropout (0.05) was applied in the second and third stages. In the *Down-sampling Module*, dropout rates of 0.1 and 0.15 were used in the early and late convolutional blocks, respectively (see Sec. S1.5).

We applied random Gaussian noise to the input data during training across all models for identity verification. The noise was added independently to each sample by scaling normally distributed random values with the corresponding percentage of intensities. Exactly, for each encoded measurement $\mathbf{C}$, we generated noise $\epsilon \sim \mathcal{N}(0,1)$ of the same shape and scaled it element-wise as $\epsilon \cdot (\gamma_g \cdot \mathbf{C})$ where γ_g controls the relative noise level. In all our experiments, we used $\gamma_g = 0.1$.

We employed channel-wise brightness augmentation during training. For each encoded measurement $\mathbf{C}$, the brightness in every channel k was randomly scaled by a factor $\mu_{b,k} \sim U(1-\gamma_b, 1+\gamma_b)$ where γ_b controls the maximum relative change. In all our experiments, we fixed $\gamma_b = 0.1$.

We further applied channel-wise contrast augmentation during training. For each encoded measurement $\mathbf{C}$, the mean intensity of each channel $\overline{\mathbf{C}}_k$ was first computed as $\overline{\mathbf{C}}_k = \frac{1}{|\Omega|} \sum_{\mathbf{u}\in\Omega} \mathbf{C}_{k,\mathbf{u}}$, where Ω denotes the set of all pixels in measurement $\mathbf{C}$. The contrast in channel k was then randomly scaled by a factor $\mu_c \sim U(1-\gamma_c, 1+\gamma_c)$ and applied as $\mathbf{C}'_{k,\mathbf{u}} = (\mathbf{C}_{k,\mathbf{u}} - \overline{\mathbf{C}}_k)\mu_c + \overline{\mathbf{C}}_k$ where γ_c controls the strength. In all our experiments $\gamma_c = 0.1$.

S1.10. Complete Results of CNN Embedding Encoders

In this section, complete results of experiments with CNN embedding encoders are presented in Table S8.

						$c_{\cos}(\overline{\mathbf{u}}_c, \overline{\mathbf{s}}_c)$				$\text{FCN}(\mathbf{u}, \mathbf{s})^{+}_{\cos}$			
				no registration		$\mathcal{R}^{(22)}$		$\mathcal{R}^{(24)}$		$\mathcal{R}^{(22)}$		$\mathcal{R}^{(24)}$	
	κ	w	C	AUROC	TPR@5%	AUROC	TPR@5%	AUROC	TPR@5%	AUROC	TPR@5%	AUROC	TPR@5%
custom CNN	G	U	3	88.3±3.8	52.4± 9.3	87.2±4.2	47.1± 8.0	87.3±3.5	48.6± 7.1	84.6±4.5	42.9± 6.8	83.4± 4.5	40.5± 7.8
custom CNN	G	U	5	89.0±2.6	50.4± 8.7	88.0±3.5	50.7± 7.9	87.2±3.2	50.2± 6.7	85.8±3.4	46.5± 5.5	84.4± 3.7	41.1± 6.2
custom CNN	G	U	10	88.7±3.9	53.7± 9.7	86.2±4.2	46.0±10.0	85.8±4.2	43.6± 9.2	82.2±5.2	38.2± 8.6	83.2± 5.1	39.2± 8.5
custom CNN	G	U	20	89.0±3.7	53.1± 7.1	87.5±3.9	49.0± 6.6	87.9±3.0	50.3± 6.6	84.9±3.9	43.6± 5.6	84.2± 4.8	43.4± 7.1
GoogLeNet	G	U	3	87.1±3.2	43.9± 6.9	86.5±4.0	44.4± 7.7	86.6±3.7	43.8± 7.7	84.1±4.4	34.9± 8.6	84.8± 4.3	35.6± 9.4
Inception-v3	G	U	3	86.0±3.5	40.2± 5.6	85.5±3.3	39.2± 5.0	85.5±3.5	40.2± 5.1	83.5±3.9	32.8± 6.8	84.0± 4.0	34.3± 9.1
ResNet-101	G	U	3	85.5±3.2	39.1± 8.2	85.4±3.3	37.0± 4.6	85.5±3.5	37.5± 6.4	84.3±4.0	33.1± 6.6	84.7± 4.4	33.5± 8.7
ResNet-18	G	U	3	87.4±3.2	43.3± 6.5	86.6±3.1	40.6± 5.9	86.9±3.0	41.1± 5.9	84.7±4.0	33.6± 7.3	85.2± 4.1	33.5± 7.7
VGG16	G	U	3	75.0±7.6	46.6±12.2	78.3±9.8	41.9± 9.4	78.4±9.9	42.2± 8.9	73.8±7.4	27.6±11.2	73.8± 7.7	26.6± 8.2
custom CNN	G	I	3	84.2±7.8	44.6±13.7	88.2±2.9	50.8± 5.1	86.7±3.9	46.8± 8.0	84.0±4.5	40.5± 5.6	83.8± 5.1	40.0± 7.8
custom CNN	G	I	5	89.5±3.4	53.3± 8.3	88.3±3.4	51.3± 6.5	88.4±3.4	50.7± 6.7	85.6±4.4	43.5± 7.5	85.4± 3.8	43.9± 6.2
custom CNN	G	I	10	83.6±5.2	38.9±12.2	87.0±4.1	43.2± 8.4	84.5±5.2	41.6± 8.7	83.0±4.7	36.8± 9.8	83.3± 4.9	39.5± 8.3
custom CNN	G	I	20	84.7±4.1	48.1± 3.4	87.1±2.9	49.5± 5.8	86.1±4.7	48.1± 5.5	88.5±1.1	53.6± 2.3	87.0± 4.1	46.2± 1.7
GoogLeNet	G	I	3	87.9±3.5	46.8± 7.7	86.8±3.9	44.3± 8.4	86.7±3.4	44.7± 7.5	85.0±3.8	35.2± 8.9	84.9± 4.1	36.1±10.3
Inception-v3	G	I	3	85.4±3.5	43.0± 9.0	84.3±3.6	39.8± 5.6	84.5±3.7	40.6± 6.2	82.6±3.9	32.4± 9.1	82.8± 3.7	33.6±10.8
ResNet-101	G	I	3	86.3±4.1	41.5±11.4	86.0±4.2	38.5± 8.7	86.5±4.1	40.6± 7.7	84.5±4.7	35.3± 8.7	84.9± 4.4	35.2± 9.1
ResNet-18	G	I	3	87.5±3.9	44.9± 8.8	87.3±3.5	42.9± 5.2	86.9±3.2	41.9± 5.9	85.2±3.8	36.1± 7.1	85.5± 4.3	36.2± 8.2
VGG16	G	I	3	76.5±7.3	47.3±12.9	79.5±9.6	42.9±10.4	79.8±9.4	42.2± 9.4	74.6±7.2	26.2± 8.3	74.5± 6.9	26.6± 6.6
custom CNN	Δ	U	3	55.4±4.9	3.4 ± 4.2	55.6±5.3	3.3 ± 4.2	55.7±4.5	3.8 ± 3.6	55.5±5.0	3.3 ± 3.5	55.6± 4.8	3.5 ± 3.9
custom CNN	Δ	U	5	55.5±4.6	3.4 ± 4.3	55.6±5.5	3.5 ± 4.3	55.4±4.7	3.4 ± 3.8	54.9±4.4	3.6 ± 3.7	55.0± 3.8	3.3 ± 3.8
custom CNN	Δ	U	10	55.4±4.7	3.7 ± 4.1	55.3±4.9	3.6 ± 4.2	54.8±4.3	3.2 ± 3.9	55.4±4.2	3.9 ± 4.5	55.7± 5.1	3.2 ± 3.7
custom CNN	Δ	U	20	55.8±5.7	3.6 ± 4.5	55.1±4.2	3.7 ± 3.8	55.7±5.1	3.8 ± 4.7	54.8±4.0	3.4 ± 4.2	55.0± 4.2	3.4 ± 3.8
GoogLeNet	Δ	U	3	53.0±3.0	1.2 ± 1.7	52.9±2.7	1.2 ± 1.4	53.2±3.3	1.7 ± 2.0	52.9±3.0	1.3 ± 1.6	53.0± 3.1	1.3 ± 1.6
Inception-v3	Δ	U	3	56.0±5.4	3.4 ± 4.2	55.9±5.3	3.3 ± 4.2	56.0±5.1	3.6 ± 3.8	55.6±5.0	3.2 ± 3.6	55.9± 5.3	3.4 ± 4.0
ResNet-101	Δ	U	3	52.8±2.5	1.2 ± 1.7	52.6±2.3	1.2 ± 1.4	52.6±2.5	1.7 ± 2.0	52.4±2.1	1.3 ± 1.6	56.1±11.1	5.0 ±11.5
ResNet-18	Δ	U	3	51.9±1.9	0.7 ± 0.8	51.9±1.8	0.8 ± 0.9	52.1±2.4	1.2 ± 1.8	51.9±1.9	0.9 ± 0.9	52.1± 2.4	0.9 ± 1.2
VGG16	Δ	U	3	52.4±2.3	1.3 ± 1.7	52.5±2.3	1.2 ± 1.4	52.6±2.9	1.9 ± 1.9	52.4±2.4	1.5 ± 1.5	52.7± 2.8	1.4 ± 1.5
custom CNN	Δ	I	3	83.1±8.4	42.9±13.7	81.0±5.1	35.2± 6.8	80.4±4.7	36.2± 5.0	78.7±5.9	31.8± 6.6	77.8± 6.1	29.8± 7.6
custom CNN	Δ	I	5	82.3±7.0	43.5± 5.1	85.5±4.1	43.5± 7.4	85.4±3.6	43.9± 6.8	80.6±5.7	34.6± 9.2	77.8± 6.3	27.6± 9.7
custom CNN	Δ	I	10	87.1±1.3	51.3± 4.8	86.8±3.7	52.4± 5.9	86.3±3.9	50.0± 6.8	82.7±4.9	42.2± 8.4	81.4± 5.0	37.0± 9.6
custom CNN	Δ	I	20	82.3±5.2	37.4±10.5	81.5±3.1	51.3± 4.2	87.3±2.5	48.1± 5.1	88.1±1.1	51.2± 3.5	86.4± 2.4	49.1± 3.7
GoogLeNet	Δ	I	3	84.0±3.3	36.4± 8.0	84.1±3.8	32.2± 6.1	83.9±3.6	31.5± 6.0	82.0±3.2	25.3± 7.1	81.7± 3.1	23.3± 5.3
Inception-v3	Δ	I	3	83.4±3.4	35.7± 8.4	82.5±3.8	28.7±10.3	83.0±3.5	28.4± 8.5	79.6±3.6	24.1± 9.1	79.7± 3.3	22.7± 8.6
ResNet-101	Δ	I	3	86.0±3.4	40.4± 9.7	83.6±2.9	32.5± 4.8	83.5±3.3	32.6± 6.0	81.7±1.8	27.2± 4.1	81.4± 1.9	27.7± 4.1
ResNet-18	Δ	I	3	83.5±4.1	33.3± 9.8	83.0±4.3	26.2± 9.4	83.0±3.9	26.4± 9.5	80.6±3.9	21.4± 7.6	81.0± 3.9	21.2± 7.9
VGG16	Δ	I	3	77.0±4.6	40.5± 6.6	77.4±3.4	38.1± 5.9	77.4±3.4	38.0± 6.0	71.7±2.7	25.1± 3.4	70.8± 2.8	25.2± 3.6

Table S8. All cross-validation Area Under ROC Curve and TPR@5%FPR results for five spatial-alignment strategies on channel representation (Sec. 3.2) of 2D Gas Chromatography Mass Spectrometry measurements on Human Scent Dataset (Sec. 4). Results reported as $\mu \pm \sigma$ across 10 folds. Identity verification performed with: (i) custom-designed Convolutional Neural Network (CNN), and (ii) five pre-trained neural network backbones *ResNet-18* [10], *ResNet-101* [10], *VGG-16* [32], *Inception-v3* [34], and *GoogLeNet* [34] with appended and trained projection layer. Registration performed with weighted cosine $c_{\cos}(\overline{\mathbf{u}}_c, \overline{\mathbf{s}}_c)$ and fully convolutional-based $\text{FCN}(\mathbf{u}, \mathbf{s})^{+}_{\cos}$ compound peak detectors introduced in [11] with 22 and 24 detected compounds. Gaussian κ_G and triangular κ_Δ channel representation kernels were used with uniform U and inversed-intensity I weightings for representation learning, number of channel representation kernels $C \in \{1, 5, 10, 20\}$.